Ocean Systems Engineering, *Vol. 10, No. 4 (2020) 399-414*
DOI: https://doi.org/10.12989/ose.2020.10.4.399

Time-domain coupled analysis of curved floating bridge under wind and wave excitations

Chungkuk Jin*, MooHyun Kim[a], Woo Chul Chung[b] and Do-Soo Kwon[c]

Department of Ocean Engineering, Texas A&M University, 727 Ross St, College Station, TX 77843, USA

(Received September 11, 2020, Revised November 28, 2020, Accepted December 2, 2020)

Abstract. A floating bridge is an innovative solution for deep-water and long-distance crossing. This paper presents a curved floating bridge's dynamic behaviors under the wind, wave, and current loads. Since the present curved bridge need not have mooring lines, its deep-water application can be more straightforward than conventional straight floating bridges with mooring lines. We solve the coupled interaction among the bridge girders, pontoons, and columns in the time-domain and to consider various load combinations to evaluate each force's contribution to overall dynamic responses. Discrete pontoons are uniformly spaced, and the pontoon's hydrodynamic coefficients and excitation forces are computed in the frequency domain by using the potential-theory-based 3D diffraction/radiation program. In the successive time-domain simulation, the Cummins equation is used for solving the pontoon's dynamics, and the bridge girders and columns are modeled by the beam theory and finite element formulation. Then, all the components are fully coupled to solve the fully-coupled equation of motion. Subsequently, the wet natural frequencies for various bending modes are identified. Then, the time histories and spectra of the girder's dynamic responses are presented and systematically analyzed. The second-order difference-frequency wave force and slowly-varying wind force may significantly affect the girder's lateral responses through resonance if the bridge's lateral bending stiffness is not sufficient. On the other hand, the first-order wave-frequency forces play a crucial role in the vertical responses.

Keywords: floating curved bridge; elastic dynamic response; coupled dynamics; bending stiffness; pontoon; wave and wind excitations; resonance; second-order wave excitation

1. Introduction

Innovative floating structures, such as floating bridge and submerged floating tunnel, have recently been suggested for deep-water and long-distance crossing. In particular, these structures can be an alternative solution to the conventional bridge, especially when the seabed is too soft or the water depth is too deep. The floating bridge is a proven structure since such bridges already exist globally, including the USA, Norway, Japan, Canada, Australia, and Guyana. Nevertheless, there are

*Corresponding author, Ph.D., E-mail: jinch999@tamu.edu
[a] Professor, E-mail: m-kim3@tamu.edu
[b] Ph.D. Candidate, E-mail: kracus83@tamu.edu
[c] Researcher, E-mail: dskwon7752@tamu.edu

http://www.techno-press.org/?journal=ose&subpage=7 ISSN: 2093-6702 (Print), 2093-677X (Online)

some issues related to their dynamic behaviors under environmental loads, which should be evaluated carefully.

Many researchers have studied the elastic behaviors of floating bridges under different environmental loadings. For example, Cheng *et al.* (2018) studied a curved floating bridge suggested for Bjørnafjorden in Norway and investigated the influences of linear and nonlinear wave forces and viscous drag force on its dynamic behavior. Xu *et al.* (2017) investigated the floating bridge's dynamic motions under wind and wave excitations while validating their time-domain model with a multi-mode flutter analysis in the frequency domain. Jin *et al.* (2020) evaluated the straight floating bridge's dynamic behaviors with mooring lines under wind and wave excitations and steady current. Petersen and Øiseth (2017) proposed a sensitivity method to update the finite element model and tuned the various system parameters to reduce the difference in natural frequencies and mode shapes between numerical and physical models. Viuff *et al.* (2016) explained how stochastic theory could be employed to incorporate the randomness of sea state into a floating bridge's design. Giske *et al.* (2017) applied the first- and second-order reliability methods to efficiently obtain the approximate solutions for floating bridge's long-term extreme responses. Fu and Cui (2012) conducted model tests for a floating bridge to evaluate its dynamic behaviors under moving loads. Wu and Shih (1998) studied the coupled motion and elastic vibration of a moored floating bridge under the moving load.

Until now, several structural types have been suggested for the floating bridge, and geometric and environmental conditions mainly govern the selection. The major environmental conditions include water depth and width, wave height and period, and current and wind velocities. The floating bridge with continuous rectangular pontoons positioned by a mooring system is one of the oldest and most popular designs. It is regarded as a proven design based on its service life. However, it might not be an optimal design in that (1) the continuous pontoons have a tendency to receive large wave and current forces over the entire length of the pontoon, so structurally significantly burdened, (2) an excessive amount of ballast is needed to compensate its buoyancy, (3) tidal variation can induce considerable fluctuations in mooring tension, (4) there is no space for the passage of ships. In this regard, a discrete-pontoon-based floating bridge has been proposed and widely studied.

This study investigates the hydrodynamic responses of a curved floating bridge with discrete pontoons through the time-domain coupled dynamics simulation. In Sections 2 and 3, the bridge design and detailed time-domain formulations are introduced. The present floating bridge is similar to the design proposed for crossing Bjørnafjorden in Norway (Larsen 2016a, b). It consists of a bridge girder, pontoons, and columns. A cable-stayed bridge in the left-end portion was not modeled in the current study for modeling simplicity. The hydrodynamic coefficients and excitation forces were obtained for the pontoons by a potential-theory-based 3D diffraction/radiation program in the frequency domain. The subsequent time-domain equation of motion is based on the Cummins equation. The bridge girder and columns were modeled by the beam element and finite element formulation. A specially devised connection method called the dummy-connection-mass method was employed to connect neighboring components in an effective manner (Jin *et al.* 2021, Jin and Kim 2018, 2020). In Section 4, environmental conditions with the method of time-history generations are explained. Wind and wave excitations and steady ocean currents were taken into consideration. In Section 5, a series of results are systematically analyzed under different loading combinations and varying bending stiffness to investigate the relationship between the system's natural frequencies and environmental loadings.

2. Bridge design

Fig. 1 shows the overall configuration of a curved floating bridge. Tables 1 and 2 summarize key design parameters. The proposed design is similar to the model suggested for crossing Bjørnafjorden in Noway. The detailed geometry and structural properties can also be available in Ref (Larsen 2016a). The girder's total length is 3940 m. 19 pontoons are equally spaced along the bridge girder, and the distance between adjacent pontoons is 197 m. Pontoon's length, height, and draft are 68 m, 14.5 m, and 10.5 m, respectively. At the pontoon's bottom, a damping plate with a thickness of 0.5 m is installed to reduce the heave, roll, pitch motions. Besides, two circular hollow columns made of steel are positioned at the top of each pontoon to support the bridge girder. Their diameter and length are 8 m and 7.5 m, respectively. Two columns are 37 m apart and arranged perpendicular to the girder's axial direction. For example, two columns are aligned parallel to the y-axis at the mid-length since the girder's axial direction is parallel to the positive x-axis. Also, the bridge girder made of steel and concrete is positioned at the top of the columns. As given in Table 2, there are two girder types, i.e., S1 and F1 types. The S1 type, consisting of plates thicker than the F1 type, is placed in the connection location with columns. Other locations are modeled with the F1 type. Abutments are located at both ends of the girder so that the fixed-fixed boundary condition can be assumed there.

Several modeling differences exist between the original design given in Ref (Larsen 2016a) and the current one. First, the cable-stayed bridge at the left-end portion is not considered here for simplicity. Second, although slightly higher and lower bridge sections exist in the original bridge design for ship traffic, we modeled a same-height bridge.

Both straight and curved floating bridges were designed for crossing Bjørnafjorden, as presented by Larsen (2016a) and Larsen (2016b). The curved floating bridge was selected in this study because of its potential advantage, i.e., no mooring is needed for the deep-water application. However, designing the structure to have excellent global performance is challenging without a mooring system. Thus, we carried out a sensitivity test regarding the girder's bending stiffness. Based on the given stiffness in Table 2, we changed bending stiffness about the strong axis (EI_Z) by 0.2 times and 1.5 times to check its effect on the girder's dynamic elastic responses.

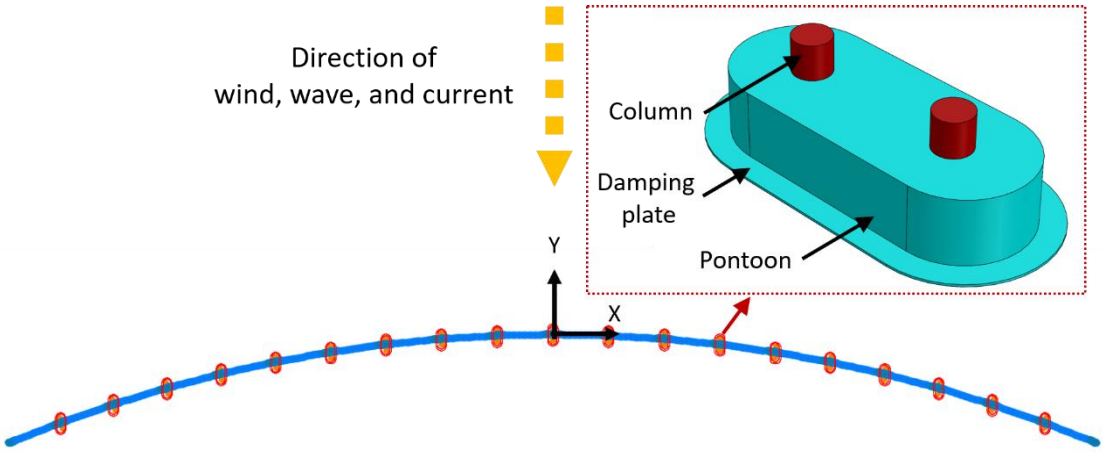

Fig. 1 Configuration of the curved floating bridge

Table 1 Design parameters of the pontoon

Item	Value	Unit
Width	28	m
Length	68	m
Height	14.5	m
Mass	11,300	t
Roll inertia	4,900,000	$t \cdot m^2$
Pitch inertia	1,360,000	$t \cdot m^2$
Yaw inertia	5,700,000	$t \cdot m^2$
Center of gravity	(0, 0, -4.2)	m
Center of buoyancy	(0, 0, -5.4)	m
Heave stiffness	17.5	MN/m
Roll water plane stiffness	5,700	MNm/rad
Pitch water plane stiffness	1,000	MNm/rad

Table 2 Design parameters of the girder and column *(E* is Young's modulus, *G* is shear modulus, *A* is the cross-sectional area, I_Y and I_Z are the second moments of area about the weak and strong axes, respectively, while I_X is the torsional second moment of area)

Item	Value			Unit
	Girder S1	Girder F1	Column	
Mass	31,800	26,712	8,000	kg/m
EI_Z	2.1×10^{14}	1.5×10^{14}	1.4×10^{12}	$N \cdot m^2$
EI_Y	3.7×10^{12}	2.6×10^{12}	1.4×10^{12}	$N \cdot m^2$
EA	5.0×10^{11}	3.7×10^{11}	1.8×10^{11}	N
GI_X	3.5×10^{12}	2.8×10^{12}	1.1×10^{12}	$N \cdot m^2$

3. Method and formulation

The time-domain coupled dynamics model for the floating bridge was built in the OrcaFlex (Orcina 2018), in which the fully-coupled interaction among pontoons, columns, and bridge girder can be solved. Time-domain equation of motion for the entire coupled system can be written as

$$\mathbf{M}\ddot{\mathbf{X}} + \mathbf{C}\dot{\mathbf{X}} + \mathbf{K}\mathbf{X} = \mathbf{F} \tag{1}$$

where **M**, **C**, and **K** are the mass, damping, and stiffness matrices, **X** and **F** are the displacement and force vectors, and the derivative of a variable is expressed by overdot. The equation of motion is solved by using the iteration-based generalized-α method (i.e., implicit scheme) (Chung and Hulbert 1993).

Pontoons interact with the surrounding fluid, and thus we need to estimate hydrodynamic coefficients and excitation forces. For that, WAMIT, the potential-flow-based 3D diffraction/radiation program (Lee 1995), was employed. In the frequency-domain, the velocity potentials are obtained by solving the boundary-value problem with the Laplace equation as governing equation and boundary conditions at the free surface, body, bottom, and far field. Added mass and radiation damping coefficients and wave excitation forces at each frequency ω are calculated from the velocity potentials. By incorporating frequency-domain results, Cummins equation expresses the time-domain equation of motion for the pontoon as

$$[\mathbf{M_P} + \mathbf{A_P}(\infty)]\ddot{\mathbf{X}}_\mathbf{P} + \mathbf{K_H}\mathbf{X_P} = \mathbf{F_1} + \mathbf{F_2} + \mathbf{F_C} + \mathbf{F_D} \tag{2}$$

where a subscript **P** stands for the pontoon, $\mathbf{A}(\infty)$ is the added mass coefficient at the infinite frequency, $\mathbf{K_H}$ is the sum of the hydrostatic and gravitational restoring coefficients, $\mathbf{F_1}$ and $\mathbf{F_2}$ are the first- and second-order wave excitation forces, $\mathbf{F_C}$ is the convolution-integral-based radiation-damping force, and $\mathbf{F_D}$ is the viscous drag force. The added mass coefficient at the infinite frequency and radiation-damping force are computed as

$$\mathbf{A_P}(\infty) = \mathbf{A_P}(\omega) + \int_0^\infty \mathbf{R}(t)\frac{\sin(\omega t)}{\omega}dt \tag{3}$$

$$\mathbf{F_C} = -\int_0^\infty \mathbf{R}(\tau)\dot{\mathbf{X}}(t-\tau)d\tau \tag{4}$$

where

$$\mathbf{R}(t) = \frac{2}{\pi}\int_0^\infty \mathbf{C_R}(\omega)\cos(\omega t)d\omega \tag{5}$$

$\mathbf{A_P}(\omega)$ and $\mathbf{C_R}(\omega)$ are the frequency-dependent added mass and radiation-damping coefficients, and **R** stands for the retardation function, obtained by conducting a Fourier cosine transform of $\mathbf{C_R}(\omega)$. In addition, the first- and second-order wave-excitation forces can be represented by the two-term Volterra series expansion as (Kim and Yue 1991)

$$F_1 = \mathrm{Re}\sum_{j=1}^{N} A_j f_j e^{-i\omega_j t} \tag{6}$$

$$F_2 = \mathrm{Re}\sum_{j=1}^{N}\sum_{k=1}^{N}\begin{bmatrix} A_j A_k^* f_{jk}^-(\omega_j,\omega_k)e^{-i(\omega_j-\omega_k)t} \\ +A_j A_k f_{jk}^+(\omega_j,\omega_k)e^{-i(\omega_j+\omega_k)t}\end{bmatrix} \tag{7}$$

where the f_j and $f_{jk}^{\pm}$ are linear and quadratic transfer functions (LTF and QTF), N is the number of sinusoidal wave components, and A is the complex wave amplitude. We did not consider second-order sum-frequency wave force since the lowest natural frequency of the present bridge is lower than the wave-frequency range. Moreover, the second-order difference-frequency wave force was

estimated by Newman's approximation. The Morison equation for a moving object computes the viscous drag force at instantaneous locations as

$$\mathbf{F_D} = \frac{1}{2} C_D \rho A_e \left| \boldsymbol{\eta}^n - \dot{\mathbf{X}}^n \right| \left(\boldsymbol{\eta}^n - \dot{\mathbf{X}}^n \right) \tag{8}$$

where C_D stands for the drag coefficients, A_e represents the area, ρ is the fluid's density, $\boldsymbol{\eta}$ is fluid's velocity, and superscript n means the normal direction. Waves and currents generate the viscous drag forces on pontoons. Considering that the distance between adjacent pontoons is 197 m, the interaction between the fluid and multi-body was not taken into consideration. So, the same hydrodynamic coefficients and wave excitation forces were inputted.

The bridge girder and columns were modeled by the finite-element-formulation-based line model in which a line consists of a series of lumped masses (nodes) and linear springs (segments). All vital physical properties such as mass and drag are lumped at the node, whereas massless springs represent the line's elastic behaviors. All external forces act on the nodes. Also, in Eq. (1), the portion of **KX** represents the line's elastic behaviors with axial, bending, and torsional springs. Axial and torsional springs that are located at the center of two adjacent nodes estimate tension and torsional moment. Shear force and bending moment are represented by rotational springs located at either side of the node. Since these components are above the water, the dynamic-wind force was solely considered, represented by the Morison equation with air density. Moreover, the static traffic force acts on the girder in the vertical direction.

Fig. 2 shows the connection methodology. All components were connected by using the dummy-connection-mass method devised for research of the submerged floating tunnel (Jin *et al*. 2021, Jin and Kim 2018, 2020). We introduced dummy rigid bodies and rotational springs to connect several objects conveniently. For translational degrees of freedom, the slave objects' positions are the same as the master's one, and thus the constraint force, i.e., the coupling force, is generated. It is similar to restricting the relative translational motions between objects by very large translational springs.

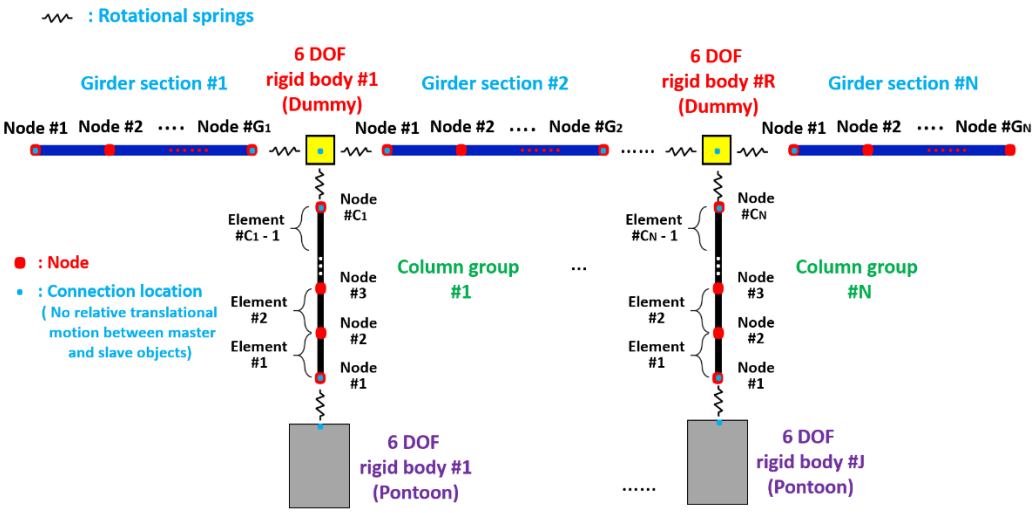

Fig. 2 Connection methodology.

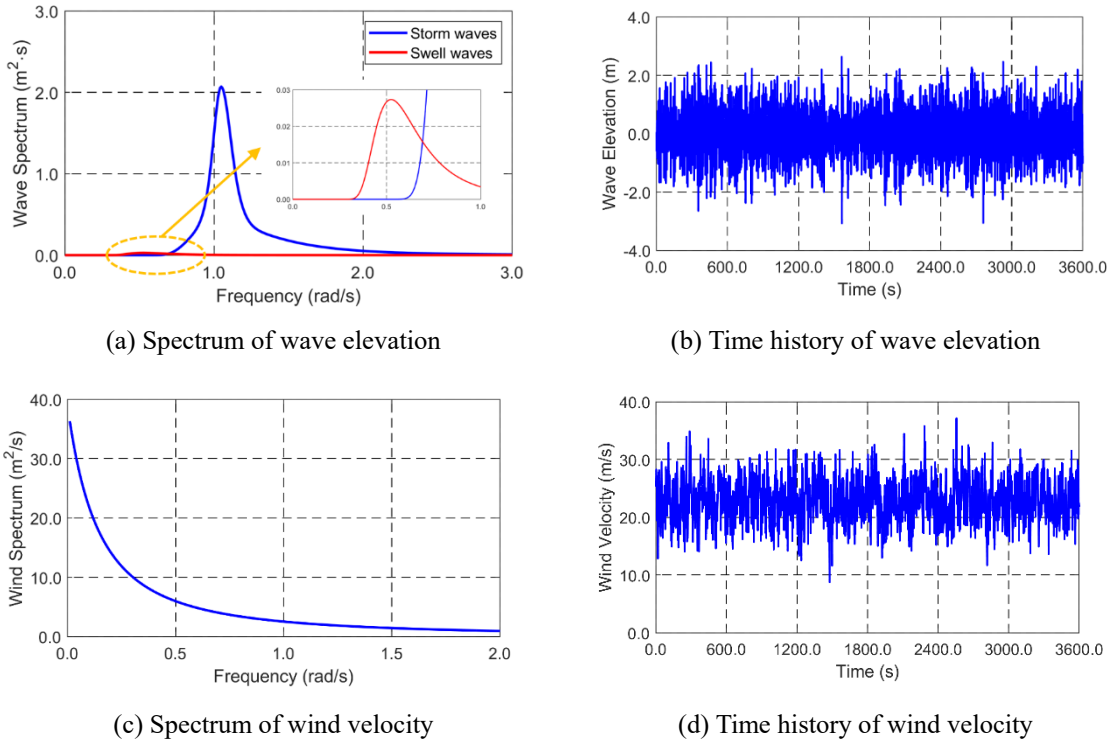

(a) Spectrum of wave elevation

(b) Time history of wave elevation

(c) Spectrum of wind velocity

(d) Time history of wind velocity

Fig. 3 Time histories and spectra of wave elevation and wind velocity

For rotational degrees of freedom, three dimensional (3D) rotational springs are employed between components. All components are rigidly coupled with large rotational springs, and there are no relative rotational motions between neighboring components at the connection location.

4. Environmental condition

We consider wind, wave, and current as environmental conditions. Both 100-year storm and ocean swell waves were considered, as shown in Fig. 3. The significant wave heights of the 100-year storm and swell waves in the Norwegian Sea are 3 m and 0.4 m, while their peak periods are 6 s and 12 s. Random waves were generated from the JONSWAP wave spectrum by superposing 100 regular wave components. Signal was prevented from repetition by using the equal energy method in which each wave component has equal spectral energy. The enhancement parameters of 5 and 1 are assumed for storm and ocean swell waves, respectively. It can be seen in Fig. 3 that the storm wave's spectral energy is much larger than the ocean swell's energy. One-year dynamic winds were generated at a mean wind speed of 22.9 m/s at 10 m height by superposing 1000 regular wind components from the API wind velocity spectrum. A constant current was taken into consideration with a current speed of 0.7 m/s. The direction of the environmental loadings was set as 270°, as depicted in Fig. 1. The simulation time was 3600 s for each case, and the time interval was 0.01 s.

Table 3 Combinations of environmental loads

Case#	First-order wave force	Second-order difference-frequency wave force	Wind force	Current force
Case 1	O			
Case 2	O	O		
Case 3	O	O	O	O

Table 4 Wet-natural frequencies and mode descriptions

Mode #	Natural frequency (rad/s)	Major direction
1	0.141	Lateral
2	0.236	Lateral
3	0.342	Lateral
4	0.430	Lateral
5	0.552	Lateral
6	0.575	Vertical
7	0.576	Vertical
8	0.576	Vertical
9	0.577	Vertical
10	0.578	Vertical

5. Results and discussions

5.1 Dynamic responses under different loading combinations

The time-domain coupled dynamics simulations of the proposed floating bridge were performed under different loading combinations to assess their influence on the bridge's global performance. We investigated the time histories, spectra, and standard deviations of the girder's dynamic responses. In specific, we checked the time histories of lateral and vertical responses at the middle-length and their standard deviations and spectra along the bridge girder. We considered three loading combinations, as presented in Table 3 (Case 1: first-order wave force, Case 2: first-order wave force and second-order difference-frequency wave force, and Case 3: first-order wave force, second-order difference-frequency wave force, wind force, and current force). The current load has a negligible influence on the dynamic responses compared with other force components.

We first performed a modal analysis after static analysis, and natural frequencies and mode shapes were analyzed. Since added mass coefficients of pontoons are frequency-dependent, an

iterative method was adopted to search the wet-natural frequencies with the added mass coefficients at respective modes, as summarized in Table 4 and Fig. 4. The wet-natural frequencies at the first lateral and vertical modes are, respectively, 0.14 rad/s (Mode #1) and 0.58 rad/s (Mode #6). Based on the modal analysis results, we can expect that the lateral motion is highly influenced by the second-order difference-frequency wave and wind forces, whereas the first-order wave force plays a significant role in the vertical motion.

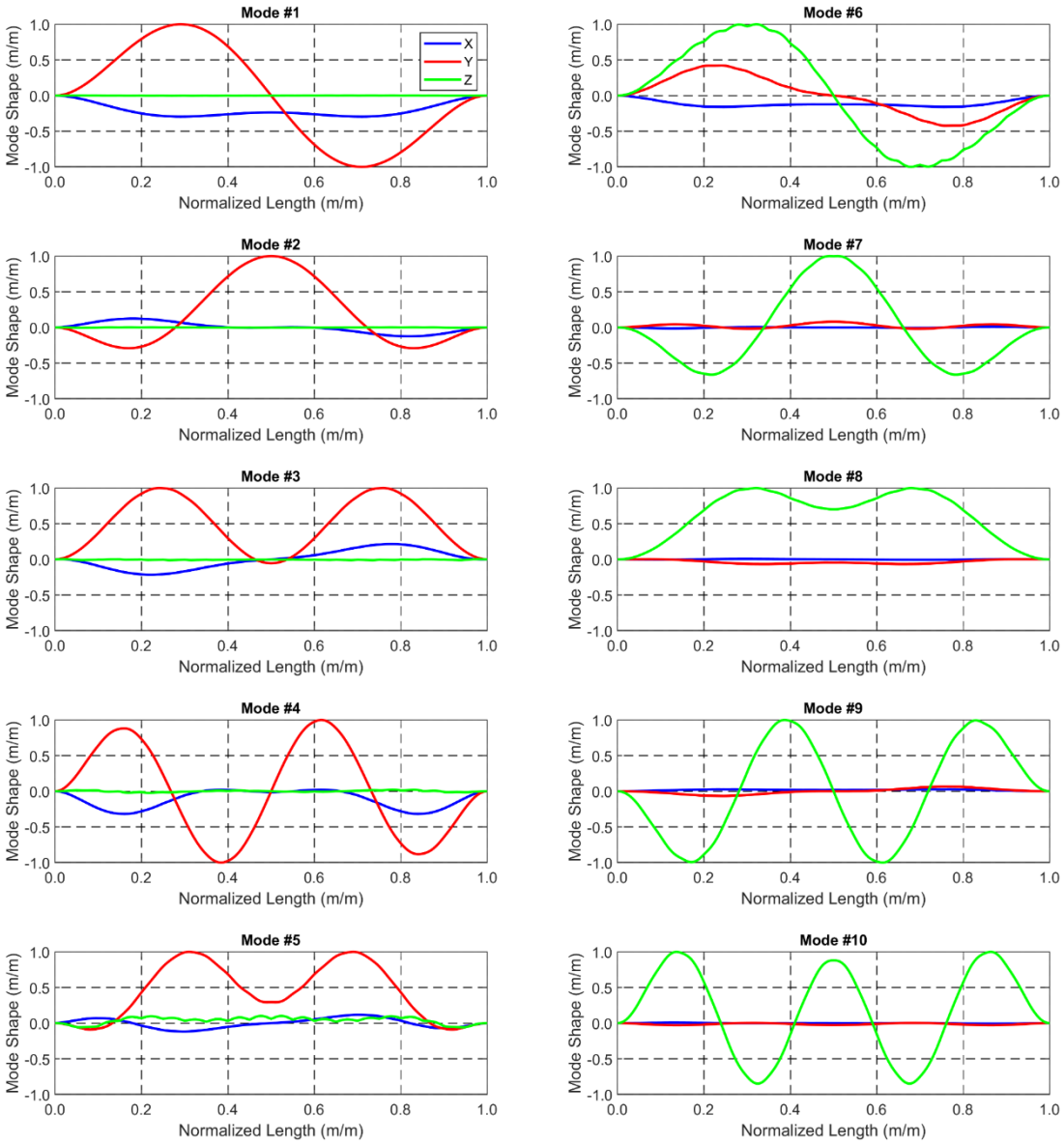

Fig. 4 Wet-mode shapes of the elastic bridge

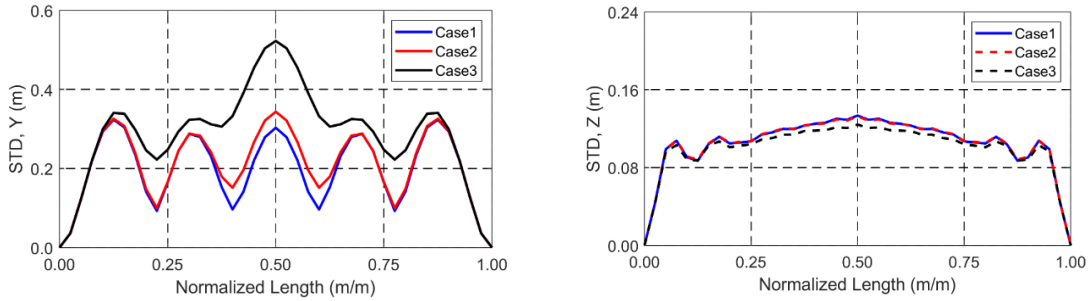

(a) (b)

Fig. 5 The STDs of the girder's lateral (a) and vertical (b) responses under different load combinations.

First, we check the standard deviations (STDs) of the girder's lateral and vertical responses along the longitudinal direction under different load combinations, as shown in Fig. 5. The lateral-response envelopes show that the high-mode-based responses are dominant for Cases 1 and 2. A slightly higher response is detected around the bridge's mid-length when additionally considering the second-order different-frequency wave force. When wind force is further employed, the STD-envelope shape similar to the second mode shape appears, and significantly increased responses can be observed at the bridge's mid-length. Since the lateral-mode natural frequencies are located in the lower frequency range way outside the wave-frequency range, the wind force plays an essential role in increasing the dynamic lateral motion. However, there are no significant variations among Cases 1-3 for the vertical responses. In this case, the first-order wave-frequency wave force plays the most critical role, whereas the second-order difference-frequency wave and wind forces become relatively insignificant. It has to be like that since the vertical-mode natural frequencies are close to swell-wave frequencies.

Next, we compare the time histories of the lateral and vertical responses at the bridge's mid-length under different load combinations, as presented in Fig. 6. Although its amplitude is small, we can see the low-frequency motion for the lateral responses as the second-order difference-frequency wave force is included in Case 2. Further including low-frequency wind force in Case 3 shows more apparent low-frequency lateral motions. As mentioned before, the natural frequencies of the lateral modes are located in the low-frequency range (i.e., natural frequencies corresponding to mode # 1-5), and thus large resonant slowly-varying lateral motions occur in addition to the wave-frequency motions. On the other hand, for the vertical responses, wave-frequency motions are dominant, and the addition of second-order wave forces and wind forces in the low-frequency range little alter the response characteristics.

Next, the corresponding spectra of the lateral and vertical motions along the longitudinal direction are investigated to further prove the relationship between the natural frequencies and motions under different load combinations, as shown in Fig. 7. For the lateral response, when only the first-order wave force is considered in Case 1, a major peak occurs at a storm peak frequency of 1.05 rad/s along with a minor peak at a swell peak frequency of 0.52 rad/s. Further consideration of the second-order difference-frequency wave force results in another small peak at 0.24 rad/s, which is induced by the resonance relevant to the second mode. As the wind force is further included, the resonant motion at 0.24 rad/s becomes dominant. The second mode's shape is similar to the spectral envelope around 0.24 rad/s, as Fig. 4 is compared with Fig. 7(e).

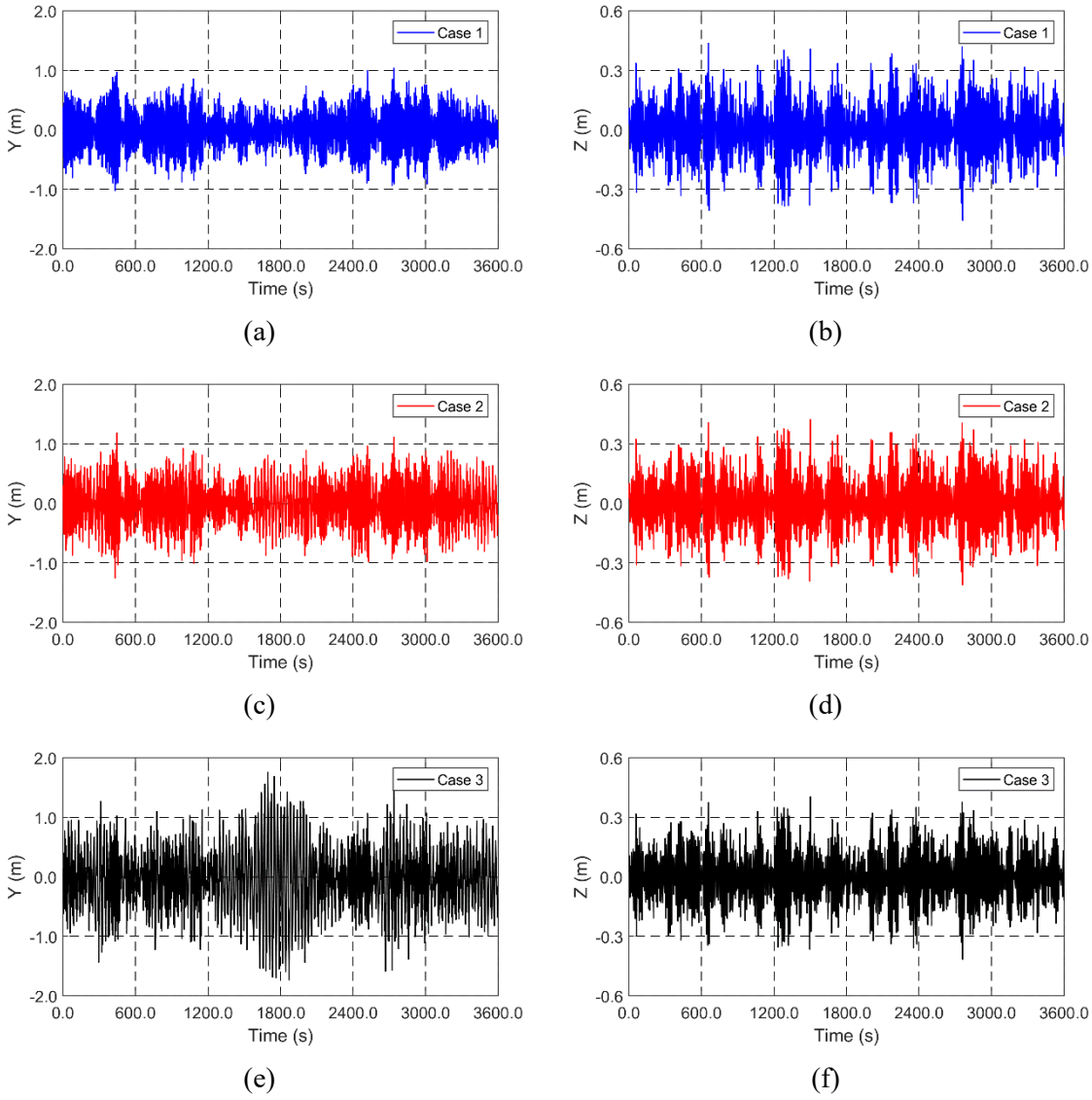

Fig. 6 Time histories of the girder's lateral and vertical responses at the bridge's mid-length under different load combinations

On the other hand, in the case of vertical responses, there seems no apparent change in the response spectra among Case 1, 2, and 3. In all cases, we observe a single dominant peak at 0.58 rad/s, which is close to the swell frequency and natural frequencies of vertical modes. Thus, even though the storm wave has much more wave energy than the swell wave, as presented in Fig. 3, the swell causes much larger elastic responses in the vertical direction. In addition, the wind force is irrelevant to the vertical response because the wind direction is lateral.

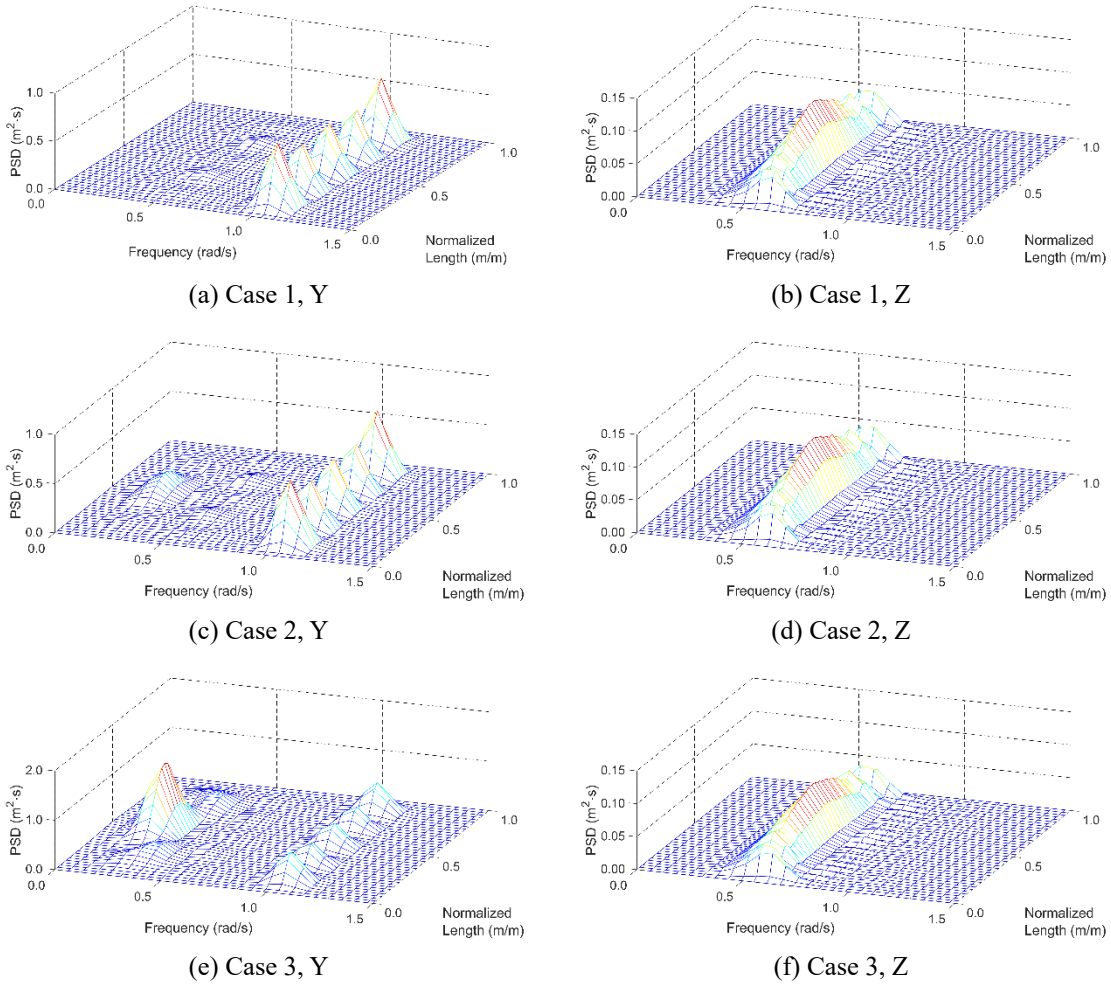

(a) Case 1, Y (b) Case 1, Z

(c) Case 2, Y (d) Case 2, Z

(e) Case 3, Y (f) Case 3, Z

Fig. 7 Spectra of the girder's lateral and vertical responses along the longitudinal direction under different load combinations

5.2 Dynamic responses at varying structural stiffness

One of the curved bridge's advantages is that mooring lines are unnecessary when sufficient bending stiffness can be provided. The curved geometry can also contribute to scatter and divert the incoming waves. Such a structure without a mooring system can make the deep-water application more plausible. According to the comparison between the straight and curved bridges proposed for crossing Bjørnafjorden in Noway (Larsen 2016a, b), the straight bridge's bending stiffness about the strong axis (EI_z) is 0.2 times that of the curved bridge, but 18 mooring lines are arranged in the straight bridge for the stationary-keeping purpose. Therefore, for a structure without mooring lines such as the curved floating bridge, sufficient bending stiffness is important for designing the bridge girder. In this regard, a sensitivity test for the girder's bending stiffness about the strong axis was carried out. We chose 0.2 *EI*, 1.0 *EI* (original design as above), and 1.5 *EI* in the sensitivity test. We only applied this stiffness variation in the

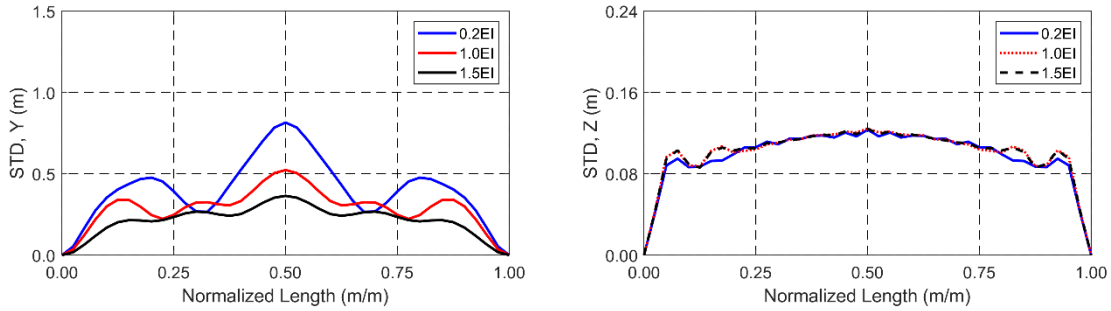

(a) (b)

Fig. 8 STD envelopes of the girder's lateral (a) and vertical (b) responses at varying bending stiffness of 0.2 *EI*, 1.0 *EI*, and 1.5 *EI*

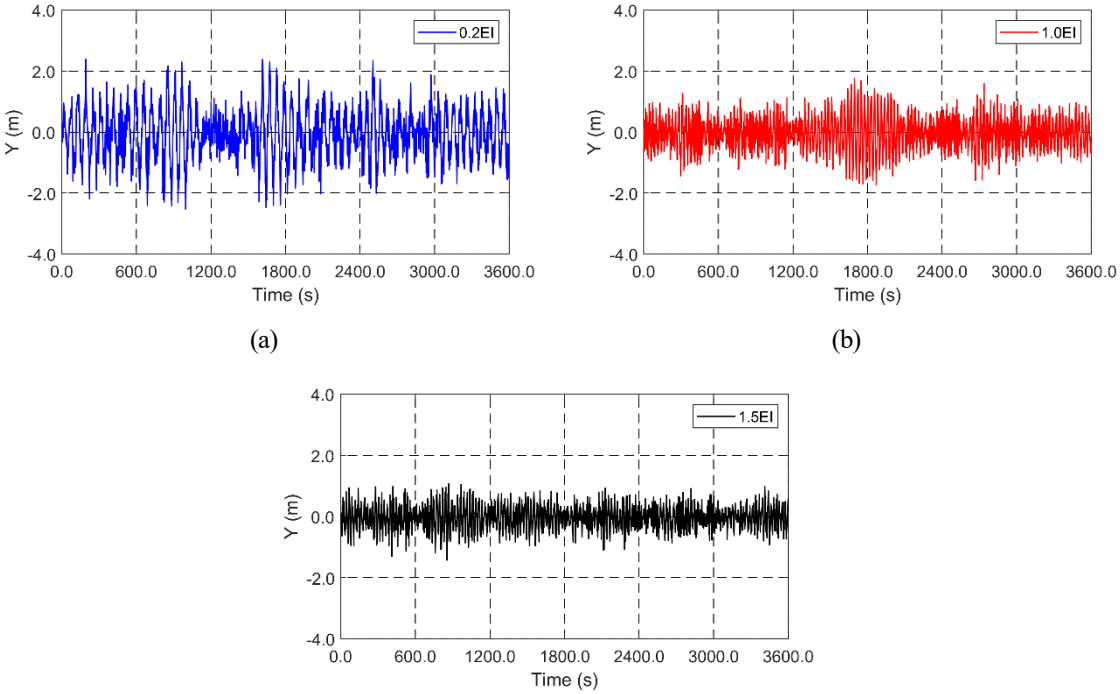

(a) (b)

(c)

Fig. 9 Time histories of the girder's lateral responses at the mid-length at varying bending stiffness of 0.2 *EI*, 1.0 *EI*, and 1.5 *EI*

strong axis, while other stiffness parameters such as torsional stiffness, axial stiffness, and bending stiffness about the weak axis were kept identical. For this purpose, Case 3 was solely taken into consideration as the most complete environmental loadings.

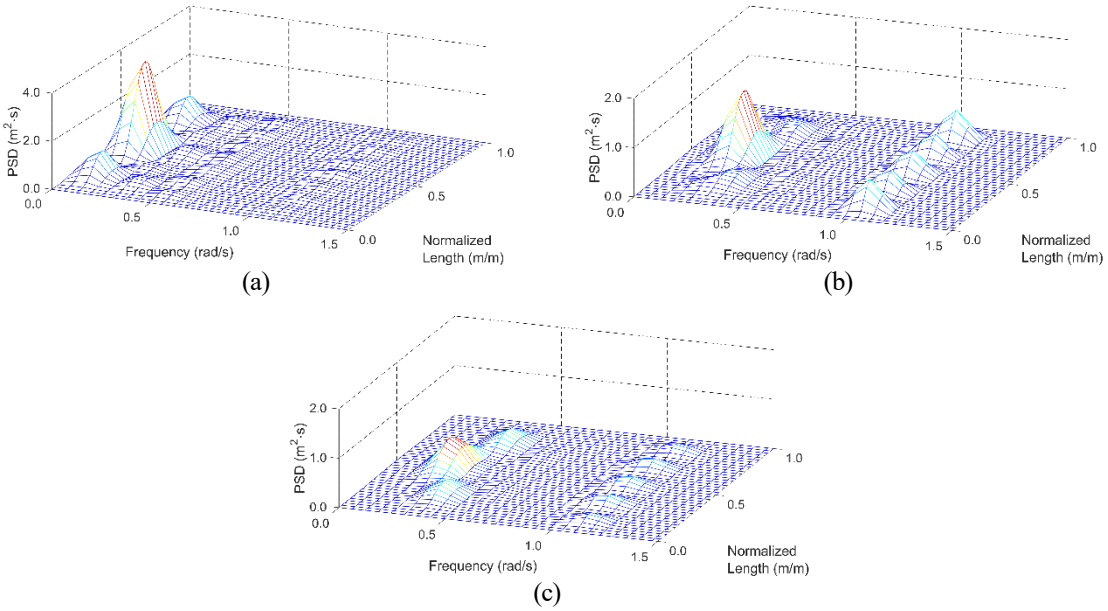

Fig. 10 Spectra of the girder's lateral responses at varying bending stiffness of 0.2 *EI* (a), 1.0 *EI* (b), and 1.5 *EI* (c)

First, the STD distributions along the bridge are compared, as presented in Fig. 8. As expected, the girder's bending stiffness is an essential factor in reducing the lateral motion. The higher the bending stiffness, the lower the standard deviation of lateral motion, especially at the bridge's mid-length. Also, the dominant mode can be determined by the shapes of envelopes. The higher mode appears for 1.0 *EI* and 1.5 *EI* cases, while lower modes govern the motion for 0.2 *EI* case. On the other hand, there is no significant variation for vertical responses since the bending stiffness about the weak axis is the same.

Next, the time histories of the lateral motions at the bridge's mid-length are compared, as shown in Fig. 9. The slow-varying resonant motion is dominant for the 0.2 *EI* case since the natural frequencies become smaller as the bridge becomes more flexible. In general, the higher the bending stiffness, the smaller the lateral motion. The resonant motion gradually decreases as the bending stiffness increases, and the wave-induced motion becomes relatively more important, as presented in Figs. 9(b) and 9(c). The reduction of low-frequency motions with increasing bending stiffness is due to more separation of the natural frequency from the significant wind energy. Wind energy is high in the low-frequency region, as demonstrated in Fig. 3(c). In the case of 0.2 *EI*, the bridge's natural frequency is closer to the significant wind energy, and thus the resulting resonant lateral motion can significantly be increased, as observed in Fig. 9(a). The corresponding lateral movements at its mid-length are not likely to be acceptable in the design.

Finally, the corresponding spectra of the lateral motions for the three *EI*s are presented in Fig. 10. Like the time-history data, the 0.2 *EI* case shows the large resonant motion at 0.11 rad/s, induced by the wind excitations. For the 1.0 *EI* case, the resonant lateral motion becomes smaller at 0.24 rad/s, and wave-induced lateral motions at 1.05 rad/s start to play some roles. For the highest *EI* case, both the resonant motions at 0.27 rad/s and wave-induced motions at 1.05 rad/s are vastly decreased. The results demonstrate that the system's bending stiffness is a critical element in the design of curved floating bridges without a mooring system.

6. Conclusions

In this study, a curved floating bridge's dynamic responses were evaluated by using the girder-column-pontoon coupled time-domain dynamics simulation program. Potential-theory-based 3D diffraction/radiation computation was carried out to estimate the pontoon's hydrodynamic coefficients and forces in the frequency domain. Those coefficients were employed in the time domain to solve the time-domain equation of motion. Besides, beam elements with finite element formulations were used to model the bridge girder and columns. The Morison equation for a moving object calculated the viscous drag force induced by winds, waves, and currents. The respective sub-components were connected by a dummy-connection-mass method with dummy 6 DOF bodies, and rotational springs were used for rotational DOFs. The constraint condition, in which the slave object strictly follows the master one, was applied to compute the constraint force between the connected bodies for translational DOFs. As the environmental conditions, dynamic winds and waves, and steady ocean currents were considered. Three loading combinations were investigated: Case 1 = first-order wave force only, Case 2 = first-order wave force and second-order difference-frequency wave force, and Case 3 = all loading components (wind force, first-order wave force, second-order difference-frequency wave force, and current force).

The girder's dynamic responses are scrutinized. Results show that the second-order wave and wind forces mainly influence the girder's lateral responses since their energies are primarily concentrated in the low-frequency region close to the system's lateral natural frequencies. On the other hand, the first-order wave force mainly influences the vertical responses as its frequency being close to the vertical-mode natural frequency. Besides, a sensitivity test with respect to the girder's bending stiffness was performed. The higher the bending stiffness, the smaller the lateral motion. The low bending stiffness case had significant resonant slowly-varying motions mainly induced by the wind excitation. The resonant motions at low frequencies were gradually reduced as bending stiffness increased due to the reduced wind energy at the increased resonance frequency.

Based on the results, special care is needed for designing a large floating bridge so that the system's natural frequency is lower than the wave peak frequency. In such a case, slowly-varying wind and second-order wave forces can play a more significant role in the elastic responses. The results demonstrate that the system's bending stiffness is a critical element in the design of curved floating bridges without a mooring system.

Acknowledgments

This work was supported by Hyundai Engineering & Construction. This work was also supported by the National Research Foundation of Korea (NRF) grant funded by the Korea government (MSIT) (No. 2017R1A5A1014883).

References

Cheng, Z., Gao, Z. and Moan, T. (2018), "Hydrodynamic load modeling and analysis of a floating bridge in homogeneous wave conditions", *Mar. Struct.*, **59**, 122-141.

Chung, J. and Hulbert, G. (1993), "A time integration algorithm for structural dynamics with improved numerical dissipation: the generalized-α method", *J. Appl. Mech.*, **60**(2), 371-375.

Fu, S. and Cui, W. (2012), "Dynamic responses of a ribbon floating bridge under moving loads", *Mar. Struct.*, **29**(1), 246-256.
Giske, F.I.G., Leira, B.J. and Øiseth, O. (2017), "Long-term stochastic extreme response analysis of floating bridges", *Procedia Eng.*, **199**, 1175-1180.
Jin, C., Bakti, F.P. and Kim, M.H. (2021), "Time-domain coupled dynamic simulation for SFT-mooring-train interaction in waves and earthquakes", *Mar. Struct*., **75**, 102883.
Jin, C. and Kim, M.H. (2018), "Time-domain hydro-elastic analysis of a SFT (submerged floating tunnel) with mooring lines under extreme wave and seismic excitations", *Appl. Sci*., **8**(12), 2386.
Jin, C. and Kim, M.H. (2020), "Tunnel-mooring-train coupled dynamic analysis for submerged floating tunnel under wave excitations", *Appl. Ocean Res.*, **94**, 102008.
Jin, C., Kim, M.H. and Chung, W.C. (2020), "Dynamic Behaviors of a Floating Bridge with Mooring Lines under Wind and Wave Excitations", *Int. J. Mech. Mechatron. Eng*., **14**(7), 240-245.
Kim, M.H. and Yue, D.K. (1991), "Sum-and difference-frequency wave loads on a body in unidirectional Gaussian seas", *J. Ship Res.*, **35**(2), 127-140.
Larsen, P. (2016a), Curved bridge-navigation channel in south, *Tech. rep., COWI and AAS-JAKOBSEN and GLOBAL MARITIME and Johs Holt as.*
Larsen, P. (2016b), Straight bridge - navigation channel in south, *Tech. rep., COWI and AAS-JAKOBSEN and GLOBAL MARITIME and Johs Holt as.*
Lee, C.H. (1995), WAMIT theory manual. *Massachusetts Institute of Technology, Department of Ocean Engineering*.
Orcina, L. (2018), OrcaFlex User Manual: OrcaFlex Version 10.2 c. *Orcina.*
Petersen, Ø.W. and Øiseth, O. (2017), "Sensitivity-based finite element model updating of a pontoon bridge", *Eng. Struct.*, **150**, 573-584.
Viuff, T., Leira, B.J., Øiseth, O. and Xiang, X. (2016), "Dynamic Response of a Floating Bridge Structure, 19th Congress of IABSE, Challenges in Design and Construction of an Innovative and Sustainable Built Environment", *The International Association for Bridge and Structural Engineering (IABSE)*.
Wu, J.S. and Shih, P.Y. (1998), "Moving-load-induced vibrations of a moored floating bridge", *Comput. Struct.*, **66**(4), 435-461.
Xu, Y., Øiseth, O. and Moan, T. (2017), "Time domain modelling of frequency dependent wind and wave forces on a three-span suspension bridge with two floating pylons using state space models", ASME 2017 36th international conference on ocean, offshore and arctic engineering. *American Society of Mechanical Engineers Digital Collection*.

PL